EXTENDED PDF FORMAT
SPONSORED BY
Travel Grants Available
AACR Annual Meeting 2014
Application Deadline:
January 31st
>Apply Now
http://www.rndsystems.com

Charge Order Driven by Fermi-Arc Instability in $Bi_2Sr_{2-x}La_xCuO_{6+\delta}$

R. Comin *et al.*

Science **343**, 390 (2014);
DOI: 10.1126/science.1242996

This copy is for your personal, non-commercial use only.

If you wish to distribute this article to others, you can order high-quality copies for your colleagues, clients, or customers by clicking here.

Permission to republish or repurpose articles or portions of articles can be obtained by following the guidelines here.

The following resources related to this article are available online at www.sciencemag.org (this information is current as of February 11, 2014):

Updated information and services, including high-resolution figures, can be found in the online version of this article at:
http://www.sciencemag.org/content/343/6169/390.full.html

Supporting Online Material can be found at:
http://www.sciencemag.org/content/suppl/2013/12/18/science.1242996.DC1.html

A list of selected additional articles on the Science Web sites **related to this article** can be found at:
http://www.sciencemag.org/content/343/6169/390.full.html#related

This article **cites 43 articles**, 7 of which can be accessed free:
http://www.sciencemag.org/content/343/6169/390.full.html#ref-list-1

This article appears in the following **subject collections:**
Physics
http://www.sciencemag.org/cgi/collection/physics

Downloaded from www.sciencemag.org on February 11, 2014

Science (print ISSN 0036-8075; online ISSN 1095-9203) is published weekly, except the last week in December, by the American Association for the Advancement of Science, 1200 New York Avenue NW, Washington, DC 20005. Copyright 2014 by the American Association for the Advancement of Science; all rights reserved. The title *Science* is a registered trademark of AAAS.

Charge Order Driven by Fermi-Arc Instability in $Bi_2Sr_{2-x}La_xCuO_{6+\delta}$

R. Comin,[1] A. Frano,[2,3] M. M. Yee,[4] Y. Yoshida,[5] H. Eisaki,[5] E. Schierle,[3] E. Weschke,[3] R. Sutarto,[6] F. He,[6] A. Soumyanarayanan,[4] Yang He,[4] M. Le Tacon,[2] I. S. Elfimov,[1,7] Jennifer E. Hoffman,[4] G. A. Sawatzky,[1,7] B. Keimer,[2] A. Damascelli[1,7]*

The understanding of the origin of superconductivity in cuprates has been hindered by the apparent diversity of intertwining electronic orders in these materials. We combined resonant x-ray scattering (REXS), scanning-tunneling microscopy (STM), and angle-resolved photoemission spectroscopy (ARPES) to observe a charge order that appears consistently in surface and bulk, and in momentum and real space within one cuprate family, $Bi_2Sr_{2-x}La_xCuO_{6+\delta}$. The observed wave vectors rule out simple antinodal nesting in the single-particle limit but match well with a phenomenological model of a many-body instability of the Fermi arcs. Combined with earlier observations of electronic order in other cuprate families, these findings suggest the existence of a generic charge-ordered state in underdoped cuprates and uncover its intimate connection to the pseudogap regime.

Since the discovery of cuprate high-temperature superconductors, several unconventional phenomena have been observed in the region of the phase diagram located between the strongly localized Mott insulator at zero doping and the itinerant Fermi-liquid state that emerges beyond optimal doping (*1*–*20*). The so-called pseudogap (PG) opens at the temperature T^* and obliterates the Fermi surface at the antinodes (ANs) of the d-wave superconducting gap function, leaving behind disconnected "Fermi arcs" centered around the nodes. In addition, charge order has been observed on the surface of Bi- and Cl-based compounds (*4*–*8*), in the bulk of La-based compounds (*9*–*11*), and most recently in $YBa_2Cu_3O_{6+\delta}$ (YBCO) (*17*–*20*), indicating that this might be the leading instability in underdoped cuprates. The similarity between the observed charge ordering wavevector and the antinodal nesting vector of the high-temperature Fermi surface has prompted suggestions that a conventional Peierls-like charge-density wave (CDW) might be responsible for the opening of the pseudogap (*7*, *8*, *12*, *19*). We used complementary bulk and surface techniques to examine the validity of this scenario and explored the connection between charge ordering and fermiology.

By applying a suite of complementary tools to a single cuprate material, $Bi_2Sr_{2-x}La_xCuO_{6+\delta}$ (Bi2201), we reveal that the charge order in this system emerges just below T^*, with a characteristic wave vector corresponding to the Fermi arc tips rather than the antinodal nesting vector. We quantified the Fermi surface by using angle-resolved photoemission spectroscopy (ARPES), and we looked for charge modulations along the Cu-O bond directions in both real and reciprocal space by using scanning-tunneling microscopy (STM) and resonant x-ray scattering (REXS). The single-layer Bi2201 is well suited to this purpose owing to (i) its two-dimensionality and high degree of crystallinity (*21*, *22*) and (ii) the possibility of probing the temperature evolution across T^*, which is better characterized (*15*, *16*) and more accessible than in bilayer systems. This study, by bringing together three different techniques on the same material belonging to the Bi family together with related observations on La- and Y-based compounds, suggests the ubiquity of charge ordering in underdoped cuprates [see also the related report for bilayer Bi2212 (*23*)].

REXS uses x-ray photons to exchange momentum with the electrons and the ionic lattice in order to gain information on the electronic charge distribution. As opposed to conventional x-ray diffraction, which is widely used for structural studies, in REXS the photon energy is tuned to resonance with one of the element-specific absorption lines. This results in a strong enhancement of the sensitivity to the valence

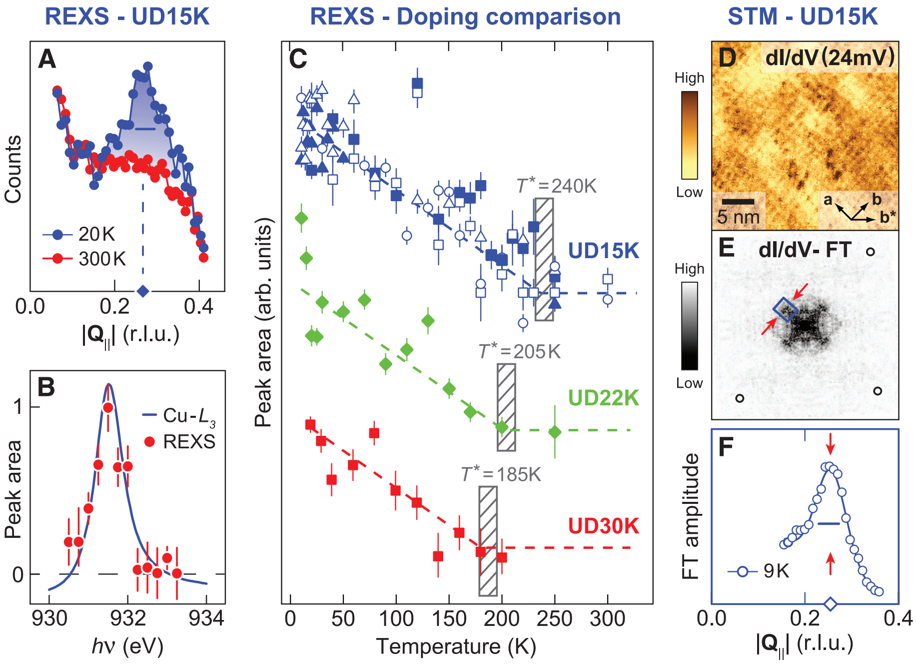

Fig. 1. REXS and STM comparison on Bi2201. (**A**) Bi2201 low- and high-temperature scans of the in-plane momentum $Q_\parallel$, showing the emergence of a CO peak around $Q_{CO} \simeq 0.265$. (**B**) Resonance profile at Q_{CO} after background subtraction (red markers), superimposed onto the Cu-L_3 absorption edge (blue line). (**C**) Temperature dependence of the CO-peak area for the three Bi2201 doping levels investigated; dashed lines are linear fits, with baseline marking the zero intensity position for each data set. Hollow and full markers for UD15K correspond to positive and negative wave vectors $Q_\parallel > 0$ and $Q_\parallel < 0$, respectively, for different samples. The PG temperature T^* (gray boxes) is from Knight shift measurements (*36*). (**D**) Bi2201 *dI*/*dV* map, taken at 24-mV bias over a 29-nm region (9 K, –200 mV, and 250 pA). A charge modulation with period $\sim 4a_0$ is seen in real space. (**E**) Fourier transform (FT) of (D), after fourfold symmetrization [black circles mark the position of the Bragg vectors (±1, 0) and (0, ±1)]. Highlighted by the blue box is the region corresponding to the line cut in (**F**), whose peak structure is suggestive of a periodic modulation with wave vector $Q_{CO} \simeq 0.248$. Horizontal bars represent half widths at half maximum.

---

[1] Department of Physics and Astronomy, University of British Columbia, Vancouver, British Columbia V6T 1Z1, Canada. [2] Max Planck Institute for Solid State Research, Heisenbergstrasse 1, D-70569 Stuttgart, Germany. [3] Helmholtz-Zentrum Berlin für Materialien und Energie, Albert-Einstein Straße 15, D-12489 Berlin, Germany. [4] Department of Physics, Harvard University, Cambridge, MA 02138, USA. [5] National Institute of Advanced Industrial Science and Technology (AIST), Tsukuba 305-8568, Japan. [6] Canadian Light Source, University of Saskatchewan, Saskatoon, Saskatchewan S7N 2V3, Canada. [7] Quantum Matter Institute, University of British Columbia, Vancouver, British Columbia V6T 1Z4, Canada.

*Corresponding author. E-mail: damascelli@physics.ubc.ca

electrons and allows the detection of very small variations in the electronic density profile within the CuO$_2$ planes (*11*), which are difficult to determine by using nonresonant methods. We performed REXS measurements along the tetragonal crystallographic **a** and **b** axes, with the corresponding reciprocal axes labeled $\mathbf{Q}_H$ and $\mathbf{Q}_K$, for three doping levels of Bi2201 (*24*). Because of the near-equivalence of $\mathbf{Q}_H$ and $\mathbf{Q}_K$, we will hereafter use the common notation $\mathbf{Q}_\parallel$ and define reciprocal lattice units (r.l.u.) for momentum axes as $2\pi/a_0 = 2\pi/b_0 = 1$, with $a_0 \simeq b_0 \simeq 3.86$Å. Figure 1A shows REXS scans at high (300 K) and low (20 K) temperatures acquired on a UD15K sample near the Cu-L_3 absorption peak at a photon energy $h\nu = 931.5$ eV. An enhancement of scattering intensity, in the form of a broad peak, is visible at 20 K at $|\mathbf{Q}_\parallel| = 0.265 \pm 0.01$, whereas at 300 K it disappears into the featureless background (dominated by fluorescence). By subtracting the latter, we can study the dependence of the low-temperature feature on photon energy, which reveals its resonant behavior at the Cu-L_3 edge (Fig. 1B). The resonant enhancement, together with the absence of features at the La-M_5 absorption edge (fig. S6), demonstrates that the peak originates from charge order (CO) occurring in the CuO$_2$ planes. Furthermore, the gradual dependence of the peak intensity on the out-of-plane component of the wavevector $Q_\perp$ is similar to observations in YBCO (*7*) and indicative of short coherence along the **c** axis. Figure 1C shows the temperature evolution of the CO peak in REXS: There is an onset temperature T_{CO}, but we cannot conclusively determine whether T_{CO} corresponds to a sharp phase boundary. Although the charge modulation breaks translational symmetry, the system lacks long-range order as evidenced by the short correlation length ($\xi_{\mathrm{CO}} \sim 20$ to 30 Å). The latter evolves only weakly with doping and temperature (fig. S5) and therefore suggests either strong disorder or substantial fluctuations persisting down to low temperatures (*25*). In either case, the convergence of T_{CO} and T^* for all doping levels suggests an intimate relationship between the CO and the PG correlations.

STM is used to detect the charge distribution in real space, by scanning an atomically sharp tip over the cleaved Bi2201 surface and mapping the differential tunneling conductance $dI/dV(\mathbf{r},V)$ (where I is current, V is potential, and $\mathbf{r}$ is position), which is proportional to the local density of states at energy $\varepsilon = eV$. Here we apply STM to the same UD15K sample studied by REXS. The map of $dI/dV(\mathbf{r},V = 24\ \mathrm{mV})$ in Fig. 1D shows an incommensurate charge modulation along the **a** and **b** axes, consistent with either a disordered checkerboard or stripe modulation (*25*). The Fourier transform of $dI/dV(\mathbf{r},V)$ (Fig. 1E) and associated line cut (Fig. 1F) quantify the CO peak at $|\mathbf{Q}_\parallel| = 0.248 \pm 0.01$. This is in good agreement with Q_{CO} from REXS and also with Q_{CO} recently reported in the context of phonon anomalies in Bi2201 (*26*). Furthermore, the feature found in STM has a correlation length $\xi_{\mathrm{CO}} \sim 28$Å, again in agreement with REXS. A summary of the REXS and STM results is presented in Table 1. We therefore arrive at the empirical convergence of a CO that onsets right below T^* (REXS) and whose wave vector is consistent on surface (STM) and bulk (REXS).

Table 1. Comparative summary for the CO peak parameters. Data from REXS and STM for the various doping levels. For ARPES, the value listed here corresponds to the observed Q_{HS}, also shown in Fig. 3C. The PG temperature T^* (gray boxes in Fig. 1C) is from Knight shift measurements (*36*). n/a, not applicable.

Technique	Sample	Parameters			
		Q_{CO} (r.l.u.)	ξ_{CO} (Å)	T_{CO} (K)	T^* (K)
REXS	UD30K ($p \simeq 0.145$)	0.243 ± 0.01	21 ± 3	180 ± 30	185 ± 10
	UD22K ($p \simeq 0.130$)	0.257 ± 0.01	23 ± 3	202 ± 20	205 ± 10
	UD15K ($p \simeq 0.115$)	0.265 ± 0.01	26 ± 3	237 ± 10	240 ± 10
STM	UD15K ($p \simeq 0.115$)	0.248 ± 0.01	28 ± 2	n/a	240 ± 10
ARPES	UD15K ($p \simeq 0.115$)	0.255 ± 0.01	n/a	n/a	240 ± 10

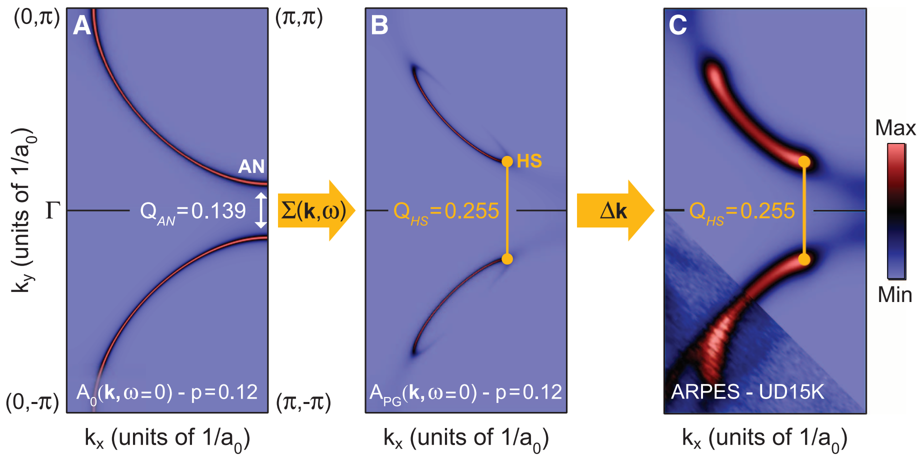

Fig. 2. ARPES and theory comparison on Bi2201. Modeled Fermi surface for hole-doping $p = 0.12$ for (**A**) the noninteracting and (**B**) the interacting case, which is computed via the inclusion of the self-energy $\Sigma_{\mathrm{PG}}(\mathbf{k},\omega)$. A further Gaussian smearing (**C**), with $\Delta k_x = \Delta k_y = 0.03\ \pi/a$ representing the effective experimental resolution, allows comparison between the calculated and measured Fermi surface from UD15K Bi2201 (*21*). The AN nesting at Q_{AN} (white arrow) can be contrasted with the Q_{HS}-vector associated with the tips of the Fermi arcs (HS), marked by the gold connector.

The next step is to link the universal surface and bulk charge order to the fermiology. We quantified and clarified this connection by using ARPES to map the Fermi surface on the same UD15K Bi2201 sample studied by REXS and STM (*21*, *22*). In a similar context, the ARPES-derived octet model in the interpretation of quasi-particle scattering as detected by STM (*27*) is a successful example of such a connection and demonstrates the importance of low-energy particle-hole scattering processes across the "pseudogapped" Fermi surface.

From the raw ARPES data (Fig. 2C) (*21*), we deduce that the charge-ordering wave vector connects the Fermi arc tips, not the antinodal Fermi surface sections, as had been assumed previously (*7*, *12*, *19*). To better understand the empirical link between charge order and fermiology, we first derived the noninteracting band structure by fitting the ARPES-measured spectral function $A_{\mathrm{exp}}(\mathbf{k},\omega)$ (where $\mathbf{k}$ and ω are electron momentum and energy, respectively) to a tight-binding model (*21*, *22*, *24*). The corresponding Fermi surface is shown in Fig. 2A for hole doping $p = 0.12$, equivalent to UD15K (*28*). The AN nesting, marked by the white arrow, yields an ordering wave vector $Q_{\mathrm{AN}} \sim 0.139$, in disagreement with the REXS/STM average value $Q_{\mathrm{CO}} \sim 0.256$. To account for the suppression of antinodal zero-energy quasi-particle excitations, a hallmark of the PG fermiology, we constructed a model spectral function $A_{\mathrm{PG}}(\mathbf{k},\omega)$ with an appropriate self-energy $\Sigma_{\mathrm{PG}}(\mathbf{k},\omega)$, which combines the features found from exact diagonalization of the Hubbard model (*29*) with the doping-dependent parameters introduced in (*30*) (see supplementary note 3 for more details). Figure 2B shows how the noninteracting Fermi surface is transformed by the action of our $\Sigma_{\mathrm{PG}}(\mathbf{k},\omega)$ and also highlights the concurrent shift in the smallest-Q zero-energy particle-hole excitation (gold connectors). The interacting

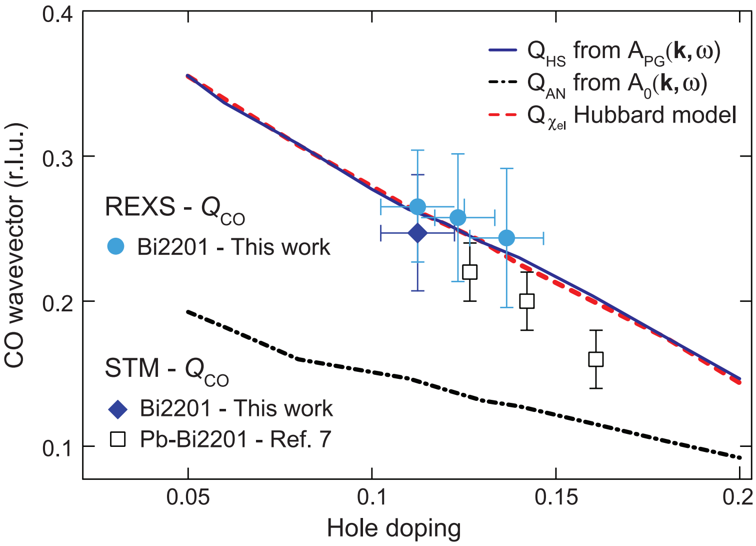

Fig. 3. Doping dependence of the CO wave vector Q_{CO}. Data from REXS and STM on Bi2201 [this work and (*7*)]; bars represent peak widths rather than errors. Also shown are the doping dependence of the Fermi surface–derived wave vectors Q_{AN} (AN nesting) and Q_{HS} (arc tips) measured from the ARPES spectral function $A_{PG}(\mathbf{k}, \omega)$, as well as the wave vector $Q_{\chi_{el}}$ from the Hubbard-model–based electronic susceptibility (*29*).

spectral function $A_{PG}(\mathbf{k}, \omega)$ used here is tuned to optimize the match with the corresponding ARPES data (*21*, *22*); after accounting for instrumental resolution, $\Delta\mathbf{k}$, the agreement with the experimental data is excellent, as shown in Fig. 2C. The vector connecting the tips of the Fermi arcs, called hot spots (HSs), is found to be $Q_{HS} \sim 0.255$, closely matching the experimental values of Q_{CO} found for the UD15K sample (see also Table 1).

In Fig. 3, we report the doping dependence of the charge-order wave vector Q_{CO} as seen experimentally, as well as Q_{AN} and Q_{HS} as obtained from the spectral functions $A_0(\mathbf{k}, \omega)$ and $A_{PG}(\mathbf{k}, \omega)$ for the noninteracting and interacting cases, respectively. The superconducting temperature–to–doping conversion for the experimental points is taken from previous studies on La-substituted Bi2201 (*28*); for Pb-substituted Bi2201 (*7*), this correspondence might be altered because Pb may contribute holes as well. The mechanism based on electron-hole scattering between AN excitations, with wave vector Q_{AN}, proves to be inadequate throughout the whole doping range. On the other hand, both the wave vector magnitude Q_{HS} and doping-dependent slope dQ_{HS}/dp agree with the Bi2201 experimental data, thereby establishing a direct connection between charge order and HS scattering. To gain further phenomenological insights into a possible link between the ordering of the electronic density and the available charge dynamics, we evaluated the momentum-dependent electronic response (susceptiblity) near the Fermi surface, or $\chi_{el}(\mathbf{Q},\Omega)$ (see supplementary note 3 for more details). We approximate $\chi_{el}(\mathbf{Q},\Omega)$ as a self-convolution of the single-particle Green's function $\mathcal{G}(\mathbf{k},\omega)$, in line with a similar approach successfully used in the study of magnetic excitations in cuprates (*31*–*33*). Despite the simplicity of our model, the results for $\mathrm{Re}\{\chi_{el}\}$ along the direction of the experimental charge-ordering confirm that there is an enhancement of particle-hole scattering at a wave vector $Q_{\chi_{el}}$ closely following Q_{HS} (dashed red line in Fig. 3). This convergence supports the idea that accounting for the empirical role played by the HSs is of critical importance for future, more quantitative studies of the electronic instability.

The convergence between the real- and reciprocal-space techniques in our study indicates a well-defined length scale and coherence associated with the electronically ordered ground state. These findings on Bi2201 suggest that the short-ranged charge correlations in Bi-based cuprates (*4*–*7*), and the longer-ranged modulations seen in Y-based (*18*, *19*, *34*, *35*) and La-based compounds (*9*–*11*), are simply different manifestations of a generic charge-ordered state [see (*23*) for related findings on Bi2212]. That the experimental ordering wave vectors can be reproduced through the correlation-induced Fermi arcs in the PG state demonstrates a quantitative link between the single-particle fermiology and the collective response of the electron density in the underdoped cuprates.

References and Notes

1. D. Bonn, *Nat. Phys.* **2**, 159–168 (2006).
2. D. Fournier *et al.*, *Nat. Phys.* **6**, 905–911 (2010).
3. A. Kaminski *et al.*, *Nature* **416**, 610–613 (2002).
4. J. E. Hoffman *et al.*, *Science* **295**, 466–469 (2002).
5. C. Howald, H. Eisaki, N. Kaneko, A. Kapitulnik, *Proc. Natl. Acad. Sci. U.S.A.* **100**, 9705–9709 (2003).
6. M. Vershinin *et al.*, *Science* **303**, 1995–1998 (2004); 10.1126/science.1093384.
7. W. D. Wise *et al.*, *Nat. Phys.* **4**, 696–699 (2008).
8. T. Hanaguri *et al.*, *Nature* **430**, 1001–1005 (2004).
9. J. M. Tranquada, B. J. Sternlieb, J. D. Axe, Y. Nakamura, S. Uchida, *Nature* **375**, 561–563 (1995).
10. M. Zimmermann *et al.*, *Europhys. Lett.* **41**, 629–634 (1998).
11. P. Abbamonte *et al.*, *Nat. Phys.* **1**, 155–158 (2005).
12. K. M. Shen *et al.*, *Science* **307**, 901–904 (2005).
13. Y. Li *et al.*, *Nature* **455**, 372–375 (2008).
14. M. J. Lawler *et al.*, *Nature* **466**, 347–351 (2010).
15. M. Hashimoto *et al.*, *Nat. Phys.* **6**, 414–418 (2010).
16. R.-H. He *et al.*, *Science* **331**, 1579–1583 (2011).
17. T. Wu *et al.*, *Nature* **477**, 191–194 (2011).
18. G. Ghiringhelli *et al.*, *Science* **337**, 821–825 (2012); 10.1126/science1223532.
19. J. Chang *et al.*, *Nat. Phys.* **8**, 871–876 (2012).
20. M. Le Tacon *et al.*, *Nat. Phys.* **10**, 52–58 (2013).
21. P. D. C. King *et al.*, *Phys. Rev. Lett.* **106**, 127005 (2011).
22. J. A. Rosen *et al.*, *Nat. Commun.* **4**, 1977 (2013).
23. E. da Silva Neto *et al.*, *Science* **343**, 393–396 (2014); 10.1126/science.1243479.
24. Materials and methods are available as supplementary materials on *Science* Online.
25. J. A. Robertson, S. A. Kivelson, E. Fradkin, A. C. Fang A. Kapitulnik, *Phys. Rev. B* **74**, 134507 (2006).
26. C. Bonnoit *et al.*, (2012), http://arxiv.org/abs/1202.4994.
27. K. McElroy *et al.*, *Nature* **422**, 592–596 (2003).
28. Y. Ando *et al.*, *Phys. Rev. B* **61**, R14956–R14959 (2000).
29. R. Eder, K. Seki, Y. Ohta, *Phys. Rev. B* **83**, 205137 (2011).
30. K.-Y. Yang, T. M. Rice, F.-C. Zhang, *Phys. Rev. B* **73**, 174501 (2006).
31. D. S. Inosov *et al.*, *Phys. Rev. B* **75**, 172505 (2007).
32. A. J. A. James, R. M. Konik, T. M. Rice, *Phys. Rev. B* **86**, 100508 (2012).
33. M. P. M. Dean *et al.*, *Phys. Rev. Lett.* **110**, 147001 (2013).
34. S. Blanco-Canosa *et al.*, *Phys. Rev. Lett.* **110**, 187001 (2013).
35. E. Blackburn *et al.*, *Phys. Rev. Lett.* **110**, 137004 (2013).
36. S. Kawasaki, C. Lin, P. L. Kuhns, A. P. Reyes, G. Q. Zheng, *Phys. Rev. Lett.* **105**, 137002 (2010).

Acknowledgments: We acknowledge S. A. Kivelson, A.-M. Tremblay, S. Sachdev, E. H. da Silva Neto, and A. Yazdani for discussions. This work was supported by the Max Planck–UBC Centre for Quantum Materials, the Killam, Alfred P. Sloan, Alexander von Humboldt, and National Sciences and Engineering Research Council (NSERC)'s Steacie Memorial Fellowships (A.D.), the Canada Research Chairs Program (A.D., G.A.S.), NSERC, Canada Foundation for Innovation (CFI), and Canadian Institute for Advanced Research Quantum Materials. J.E.H. acknowledges support from the U.S. NSF grant DMR-0847433. A.S. was funded by the A*STAR fellowship. M.M.Y. was funded by an NSERC fellowship. Part of the research described in this paper was performed at the Canadian Light Source, which is funded by the CFI, NSERC, National Research Council, Canadian Institute for Health Research, the Government of Saskatchewan, WD Canada, and the University of Saskatchewan.

Supplementary Materials

www.sciencemag.org/content/343/6169/390/suppl/DC1
Materials and Methods
Supplementary Text
Figs. S1 to S10
References (*37*–*46*)

10 July 2013; accepted 2 December 2013

10.1126/science.1242996